Nuclear Engineering and Technology 51 (2019) 176–189

Contents lists available at ScienceDirect

Nuclear Engineering and Technology

journal homepage: www.elsevier.com/locate/net

Original Article

A feasibility study on photo-production of ^{99m}Tc with the nuclear resonance fluorescence

Kwangho Ju, Jiyoung Lee, Haseeb ur Rehman, Yonghee Kim*

Department of Nuclear & Quantum Engineering, Korea Advanced Institute of Science and Technology, 291Daehak-ro Yuseong-gu, Daejeon, 34141, South Korea

ARTICLE INFO

Article history:
Received 13 July 2017
Received in revised form
6 August 2018
Accepted 4 September 2018
Available online 7 September 2018

Keywords:
Laser-Compton scattering (LCS)
Nuclear resonance fluorescence (NRF)
Tc-99 m
Energy recovery LINAC
Photo-production

ABSTRACT

This paper presents a feasibility study for producing the medical isotope ^{99m}Tc using the hazardous and currently wasted radioisotope ^{99}Tc. This can be achieved with the nuclear resonance fluorescence (NRF) phenomenon, which has recently been made applicable due to high-intensity laser Compton scattering (LCS) photons. In this work, 21 NRF energy states of ^{99}Tc have been identified as potential contributors to the photo-production of ^{99m}Tc and their NRF cross-sections are evaluated by using the single particle estimate model and the ENSDF data library. The evaluated cross sections are scaled using known measurement data for improved accuracy. The maximum LCS photon energy is adjusted in a way to cover all the significant excited states that may contribute to ^{99m}Tc generation. An energy recovery LINAC system is considered as the LCS photon source and the LCS gamma spectrum is optimized by adjusting the electron energy to maximize ^{99m}Tc photo-production. The NRF reaction rate for ^{99m}Tc is first optimized without considering the photon attenuations such as photo-atomic interactions and self-shielding due to the NRF resonance itself. The change in energy spectrum and intensity due to the photo-atomic reactions has been quantified using the MCNP6 code and then the NRF self-shielding effect was considered to obtain the spectrums that include all the attenuation factors. Simulations show that when a ^{99}Tc target is irradiated at an intensity of the order 10^{17} γ/s for 30 h, 2.01 Ci of ^{99m}Tc can be produced.

1. Introduction

Technetium-99m (^{99m}Tc), a metastable isomer of ^{99}Tc, is the most commonly used medical radioisotope in the world and can be found in over 40 million nuclear-medicine procedures every year [1]. Its short half-life of ~6 h linked with an easily detectable but relatively safe 143 keV gamma decay has made it an ideal radioisotope for medical applications. When coupled with suitable chemical compounds, it allows for the diagnosis and examination of specific physiological processes, making it essential for non-invasive medical procedures.

Currently, in order to yield ^{99m}Tc, ^{99}Mo is first produced in research reactors as a byproduct of ^{235}U fission reactions where over 90% of the world's demand has been supplied. The ^{99}Mo, with a half-life of ~66 h, then may naturally decay to ^{99m}Tc. However, most of the nuclear reactors are aged, over 45 years old, and withdrawing from active service. Moreover, highly-enriched uranium (HEU) has been traditionally used for the production of ^{99}Mo in the reactors, which provokes proliferation concerns because the ^{99}Mo has to be separated from the irradiated HEU object. As a substitution, accelerator-based approaches are mainly pursued and can be divided into fission-based and transmutation-based methods.

In fission-based methods, photo-fission production of ^{99}Mo is achieved by bombarding a high-*Z* converter target (e.g. tungsten (W) or tantalum (Ta)) with energetic electrons (i.e. 30–50 MeV) to produce gammarays. The gamma rays are then directed towards depleted uranium, low enriched uranium (LEU), or HEU where ^{99}Mo is produced through a photo-fission (γ,f) reaction. The advantage of this method lies in the large amount of ^{99}Mo that can be produced. Nevertheless, the licensing of these sub-critical nuclear systems along with the use of hot-cell processing and waste disposal are major concerns preventing the widespread use of this technology [1–3].

In transmutation-based methods, cyclotron proton accelerators are used to produce many short-living medical isotopes. However, only some are capable of producing ^{99}Mo using (p,2n) and (p,pn) reactions; none of which are suitable for producing more than a

* Corresponding author.
E-mail address: yongheekim@kaist.ac.kr (Y. Kim).

https://doi.org/10.1016/j.net.2018.09.002

small fraction of the required amounts of ^{99}Mo [1]. In addition, protons with energies in between 19–24 MeV can yield acceptable radionuclidic purity whereas energies less than 10 MeV can increase the patient doses (up to 30% or more). The patient doses can also be affected by the composition of other molybdenum isotopes [4,5].

Aforementioned methods produce ^{99}Mo to make a ^{99m}Tc generator which is milked for ^{99m}Tc. Eventually, both ^{99}Mo and ^{99m}Tc decay to ^{99}Tc, which must be disposed of with special care due to its long half-life (211,100 years) and high mobility in ground water. It is estimated that 30–40% of the produced ^{99}Mo in a ^{99m}Tc generator is not utilized and left to decay to ^{99}Tc. Furthermore, this ^{99}Tc is also independently produced in the reactors and constitutes ~0.1% of the total spent fuel inventory.

In this study, the authors investigate an innovative way to produce the useful ^{99m}Tc by recycling the hazardous ^{99}Tc [6]. The feasibility of ^{99}Tc (γ,γ')^{99m}Tc reactions is investigated in view of effectiveness of the nuclear resonance fluorescence (NRF) reaction triggered by the laser Compton scattering (LCS) photons [7,8]. The NRF reaction is commonly used for material assay because a specific radionuclide can be identified based on its NRF signature peaks. Currently, the NRF nuclear reactions can be simulated by only a few computer codes such as PHITS [9,10]. In this research, we have also calculated the NRF cross-sections with similar methods used in the PHITS code to evaluate feasibility of the photo-production of ^{99m}Tc. This paper largely focuses on the physics study of NRF-based photo-production of ^{99m}Tc with the use of optimized LCS gamma-rays.

2. Nuclear resonance fluorescence

The NRF reaction is the result of the nuclear absorption and subsequent emission of a high-energy photon. Fig. 1 illustrates the essential concept of the NRF reaction. In Fig. 1, E_0 and E_γ represent the energies of the ground and excited states of the nucleus, respectively. The E_0 state of a ^{99}Tc nucleus can be excited to E_γ with a photon whose energy is very close to E_γ-E_0. The nucleus will then stay in the excited state for a very short time (usually femtoseconds) before releasing a photon to decay to either the original E_0 or other states.

The NRF cross-section follows the Breit-Wigner formula and is given by Eq. (1):

$$\sigma(E) = \frac{1}{4\pi}\frac{2J+1}{2J_0+1}\left(\frac{hc}{E}\right)^2 \frac{\Gamma\Gamma_0}{(E-E_\gamma)^2 + I^2/4} \tag{1}$$

where J is the nucleus spin in the excited state, J_0 is the spin in the ground state, Γ is the total sum of the decay widths of all possible decay paths at the excited energy level, Γ_0 is the partial decay width from the excited to ground state, and E is the incident gamma-ray energy. In this research, the NRF cross-section is calculated using the nuclear data of ^{99}Tc based on evaluated nuclear structure data file (ENSDF) [11]. While calculating NRF cross-section, the Doppler broadening should be considered with the Breit-Wigner formula because it assumes that thermal motion does not happen in the nucleus and the reaction happens at absolute zero temperature, which is obviously impractical.

Generally, Gaussian distribution is used to express thermal motion of the nucleus. Eq. (2) denotes the Breit-Wigner formula combined with the Gaussian distribution.

$$\sigma_{eff}(E) = \int_0^\infty \sigma(E')\frac{1}{\sqrt{2\pi}\Delta} exp\left(\frac{-(E'-E)^2}{2\Delta^2}\right)dE' \tag{2}$$

where Δ is the Doppler width which can be expressed by Eq. (3):

$$\Delta = \frac{E_\gamma}{c}\sqrt{\frac{kT}{M}} \tag{3}$$

where c is the speed of the light, k is Boltzmann constant, T is the temperature of the target nucleus, and M is the nuclear mass. As the resonance peak calculated by the Breit-Wigner formula is very sharp, it can be treated as the delta function. Then, Eq. (2) can be simplified to Eq. (4):

$$\sigma_{eff}(E) = \frac{(hc)^2\Gamma_0}{4E_\gamma^2}\frac{2J+1}{2J_0+1}\frac{1}{\sqrt{2\pi}\Delta} exp\left(\frac{-(E_\gamma-E)^2}{2\Delta^2}\right) \tag{4}$$

Energy widths are derived by the half-life of the excited state which can be found in ENSDF. However, they are not given mostly for all known energy levels. Therefore, theoretical methods should be used to derive them. Although there are many models to describe the energy width, the most conventional method is the single particle estimate model by Weisskopf [12]. This model expresses the energy width using transition strengths, which are reciprocals of the mean-life time.

The transition strengths are divided into two kinds. One is an electric transition and the other is a magnetic transition. The type of the transition is decided by nuclear quantum states of the initial and final energy levels. Eq. (5) describes both types of transition strengths using the single particle estimate model:

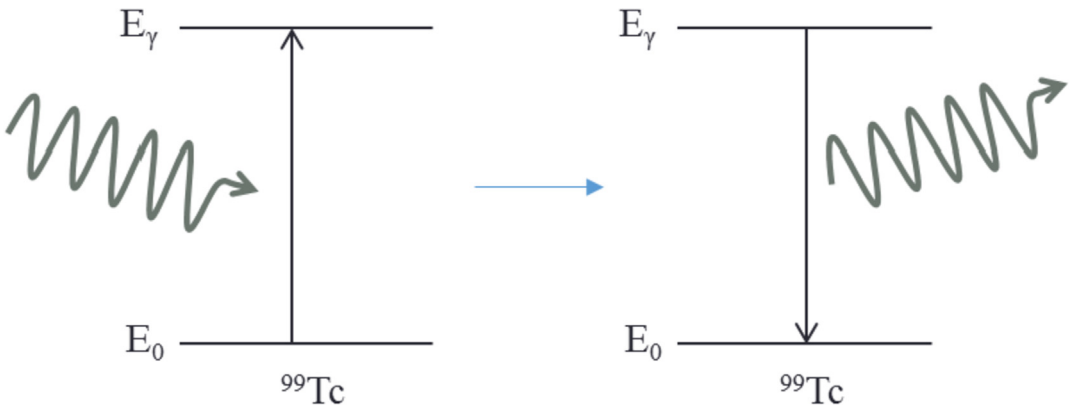

Fig. 1. The NRF reaction.

$$T_{\gamma}^{EL} = \frac{2(L+1)e^2}{L[(2L+1)!!]^2\hbar}\left(\frac{E_{\gamma}}{\hbar c}\right)^{2L+1}\left(\frac{3}{3+L}\right)^2 R^{2L},$$
$$T_{\gamma}^{ML} = \frac{80(L+1)\mu_n^2}{L[(2L+1)!!]^2\hbar}\left(\frac{E_{\gamma}}{\hbar c}\right)^{2L+1}\left(\frac{3}{3+L}\right)^2 R^{2L-2}, \quad (5)$$

where T_{γ}^{EL} is the electric transition strength, T_{γ}^{ML} is the magnetic transition strength, L is the angular momentum shift term, e is the elementary charge, μ_n is magnetic moment of the proton, R is the radius of nucleus and $\hbar$ is the reduced Planck's constant. The total transition strength can be obtained by Eq. (6):

$$T\left(L, E_{\gamma}, J_i^{\pi}, J_f^{\pi}\right) = \sum_{\mathrm{L=Max}\left(1,|J_i-J_f|\right)}^{J_i+J_f}\left(T_{\gamma}^{EL}+T_{\gamma}^{ML}\right)$$
$$T_{\gamma}^{ML} = 0, \text{if } (-1)^{\mathrm{L}}\pi_i\pi_f = +1$$
$$T_{\gamma}^{EL} = 0, \text{if } (-1)^{\mathrm{L}}\pi_i\pi_f = -1 \quad (6)$$

In. Eq. (6), π_i and π_f indicate parity of the initial and final state, respectively. It is well known that the high-order transitions ($L > 2$) are negligibly small and the transitions are usually considered only up to the second order, i.e., $L = 1$ or 2. It is also worthwhile to note that transition strength for $L = 2$ is generally 3 orders of magnitude smaller than that for $L = 1$.

Energy widths are expressed by transition strengths for all possible decay paths. The energy width is proportional to the summation of these strengths, and is given by Eq. (7):

$$\Gamma = \hbar T. \quad (7)$$

In fact, the single particle estimate model works quite well for the isotopes near the magic numbers as it assumes the nuclear properties are determined by a few nucleons while remaining nucleons produce a common potential. Meanwhile, it was found that for the isotopes other than magic number ones, model-based results should be appropriately scaled for a good agreement with the experimental values [13]. Reference [13] indicates that experimental data of ^{239}Pu can be used for scaling the magnetic transition while electric transition strength can possibly be scaled with measurements of ^{238}U. We found that the single particle estimate model provides unacceptably high NRF cross-sections for ^{99}Tc, and therefore, the scaling factor method also was introduced in this work to adjust NRF cross-sections of ^{99}Tc. The scaling factors were determined by a least-square fitting using available experimental data of ^{239}Pu and ^{238}U. It is expected that the scaled NRF cross-sections can be more reliable than the naive predictions by the standard model. In this study, only E1 and M1 transitions are adjusted though other transition types exist. This is mainly because a dipole strength is much higher than the others such as quadrupole transition in the single particle estimate model, as mentioned above. Table 1 provides the transition types between nuclear states of ^{99}Tc for 21 NRF peaks. As shown in Table 1, one can clearly note that most of the transition types are E1 or M1 dipole one.

Table 2 compares the integrated NRF cross sections of the 21 excited states before and after the scaling with experimental data of ^{238}U and ^{239}Pu. One can clearly note that the naive application of the single particle estimate model results in unacceptably high cross sections for most of the energy states, while the scaled cross sections are usually a few orders of magnitude smaller. We believe that the scaled cross-sections are rather acceptable although the associated uncertainties cannot be quantified at the moment.

Fig. 2 shows the direct excitation scheme of ^{99}Tc to ^{99m}Tc. The left-hand side numbers in Fig. 2 indicate the spin and parity of the nuclear states and those in right-hand side indicate energy levels of ^{99}Tc nucleus. The NRF cross-section for excitation directly to the desired isomeric state, ^{99m}Tc, is evaluated to be negligibly small (on the order of 10^{-15} b), which means that a direct excitation from the ground to the isomeric state is practically impossible. As a result, an indirect ^{99m}Tc production is explored at higher excited states, which is depicted in Fig. 3. The multi-step cascade is considered for a few energy states in Fig. 3, as it will be complicated to identify the cascades for all the 21 energy states. Also, we are interested only in those cascades which result in the isomeric state.

Fig. 4 shows the NRF cross-sections and total branching ratios (BR_{total}) at the excited energy levels that can result in the production of ^{99m}Tc and are available within ENSDF. Note that the BR_{total} cannot be calculated if information about the photon branching ratios is missing in the ENSDF file, even if a branching ratio to ^{99m}Tc exists. In addition, NRF cross-sections cannot be calculated if the transition path to the ground state for each excited energy level is not provided. BR_{total} and NRF cross-sections are not depicted in Fig. 4 for such cases.

In Fig. 4, 21 NRF cross-sections are shown with corresponding BRs in the energy range from 0.5 MeV to 1.6 MeV. One can see that the NRF cross-sections are quite resonance-dependent and the maximum cross-section is about 3.8 b in the vicinity 1.072 MeV. It is also noteworthy that the NRF resonance is very sharp and the peak cross-section is noticeably high for many excited states in the NRF resonances. The full width at half maximum (FWHM) of the resonances is only 1–2 eV at 300 K. Regarding the NRF cross-section in Fig. 4, it should be mentioned that the uncertainty of the current cross-section estimates is considered quite high because there is no measured data available at the moment.

Fig. 5 shows the case when the ^{99}Tc nucleus is excited to 1207 keV and then decays to 143 keV. After ^{99}Tc is excited to 1207 keV, it can decay to 143 keV through either 884 keV or 671 keV, and the probabilities of decaying to the aforementioned energy states are 29.6% and 26.8%, respectively. The branching ratio of decaying to 143 keV is 57.3% for 884 keV and 59.9% for 671 keV. We can reasonably estimate the total branching ratio for 1207 keV to decay to 143 keV by summing the product of the two possible decay paths, which in this case turns out to be 33%. As such, 33% of ^{99}Tc at 1207 keV energy level is assumed to decay to the desired 143 keV energy level via photon emission.

The NRF cross-section for the energy state of 1207 keV is 0.434 eVb. The actual NRF cross-section for 1207 keV is shown in Fig. 6. This unit is used because cross-section in barn depends on the temperature. However, the integrated cross-section in eVb is independent of temperature. This is based on the assumption that the area under the resonance cross-section is constant. It is also important to know that the cross-section peak is sharp and narrow.

3. Laser Compton scattering gamma-rays

The photonuclear excitation can be induced by using high-brightness gamma-rays generated from laser Compton scattering interactions. The laser Compton scattering (LCS) phenomenon is an elastic scattering of a low energy laser photon with a high energy electron to increase the energy of the photon (and reduce the wavelength), as roughly depicted in Fig. 7 [7,8].

Fig. 8 shows the head-on collision between a photon and an electron, and the resulting scattering angle (θ). In Fig. 8, T and T_S are the kinetic energies of the incident and scattered electrons with scattering angle ϕ, while E_L and E_γ are the energies of the incident and scattered photons. Further details on the theoretical basis of Compton scattering and related LCS parametric studies can be found in Refs. [7] and [8].

The energy of the scattered photon (E_γ) can be derived from the conservation of energy and momentum and can be expressed as a

Table 1
Transition types of ^{99}Tc excited states.

Initial states (keV)	Transition strength		Initial states (keV)	Transition strength		Initial states (keV)	Transition strength	
	Final states (keV)	Type		Final states (keV)	Type		Final states (keV)	Type
509.096	G.S*	E3	1004.07	G.S	E3	1207.26	G.S	E1
	142.684	M1		142.684	M1		181.094	E1
534.43	G.S	M3		181.094	E1		625.530	E1
	142.684	E1		534.440	E1		671.478	E2
612.37	G.S	M2		761.782	E1		884.259	M1
	142.684	E2	1072.23	G.S	M1	1320.73	G.S	E3
	509.096	M1		534.440	E2		509.096	M1
671.478	G.S	E3	1129.11	G.S	E3		612.370	M1
	142.684	M1		142.684	M1	1329.40	G.S	E1
	181.094	E1		509.096	M1		140.511	E1
	509.096	M1		671.477	M1		612.370	M1
884.259	G.S	M2	1135.04	G.S	M2		719.410	E1
	140.511	E1		181.094	E1	1405.45	G.S	M4
	181.094	E1		509.096	M1		509.096	M1
	509.096	M1		612.370	M1		671.478	M1
920.579	G.S	E4		884.260	M1	1444.13	G.S	M3
	142.684	E1	1176.48	G.S	E1		181.094	M1
	181.094	E2		612.370	E2		509.096	E1
	509.096	E1		739.213	E1		612.370	E1
	671.477	E1		986.170	M1	1552.12	G.S	M3
	761.782	E2	1198.89	G.S	E3		920.580	M1
986.17	G.S	E1		142.684	M1		1141.854	M1
	140.511	E1		181.094	E1	1604.29	G.S	E1
	181.094	E1		509.096	M1		986.190	E2
	509.096	E2				1611.38	G.S	M4
	612.370	M1					612.370	E2
	719.410	E1					884.259	E2

Table 2
Integrated NRF cross-sections before and after the scaling.

Excited states of Tc-99	Integrated Cross-section theoretically	Integrated Cross-section After scaling	Excited states of Tc-99	Integrated Cross-section theoretically	Integrated Cross-section After scaling
(keV)	(eV·barn)	(eV·barn)	(keV)	(eV·barn)	(eV·barn)
509.1	1.19E+01	2.38E-01	1135.04	1.89E+03	2.19E-01
534.43	9.41E+02	2.59E-02	1176.48	3.64E+04	1.05E+00
612.37	5.19E-01	1.03E-02	1198.89	5.09E+03	9.59E-01
671.48	1.73E+03	2.61E-01	1207.26	1.46E+04	4.34E-01
884.259	1.08E+04	4.16E-01	1320.732	4.54E+01	9.09E-01
920.58	1.55E-03	1.55E-03	1329.404	2.94E+04	1.34E+00
986.17	8.14E+01	2.64E-03	1405.454	1.01E+01	2.02E-01
1004.07	3.93E+02	4.72E-02	1444.134	4.00E+03	2.07E+00
1072.23	2.69E+02	5.37E+00	1552.12	6.56E+00	1.31E-01
1129.105	3.09E+00	6.19E-02	1604.287	8.61E+04	2.37E+00
			1611.376	2.90E-02	7.99E-07

function of E_L and θ as shown in Eq. (8):

$$E_\gamma = \frac{(1+\beta)E_L}{1-\beta\cos\theta + E_L/mc^2\sqrt{1-\beta^2}(1+cos\theta)} \quad (8)$$

where β is the ratio between the electron and light velocities and is given by Eq. (9):

$$\beta = \frac{\sqrt{T(T+2mc^2)}}{T+mc^2} \quad (9)$$

where mc^2 is the electron energy at rest. A key point drawn from Eq. (8) is that the scattering angle should be small (approaching the backscattering angle) to produce a high energy LCS photon.

3.1. Characteristics of the LCS reaction cross-section

The mathematical formulation of the differential Compton scattering cross-section in the electron rest (ER) frame of reference is based on the Klein-Nishina cross-section [3]. This model can then be translated to the laboratory frame and is expressed in Eq. (10):

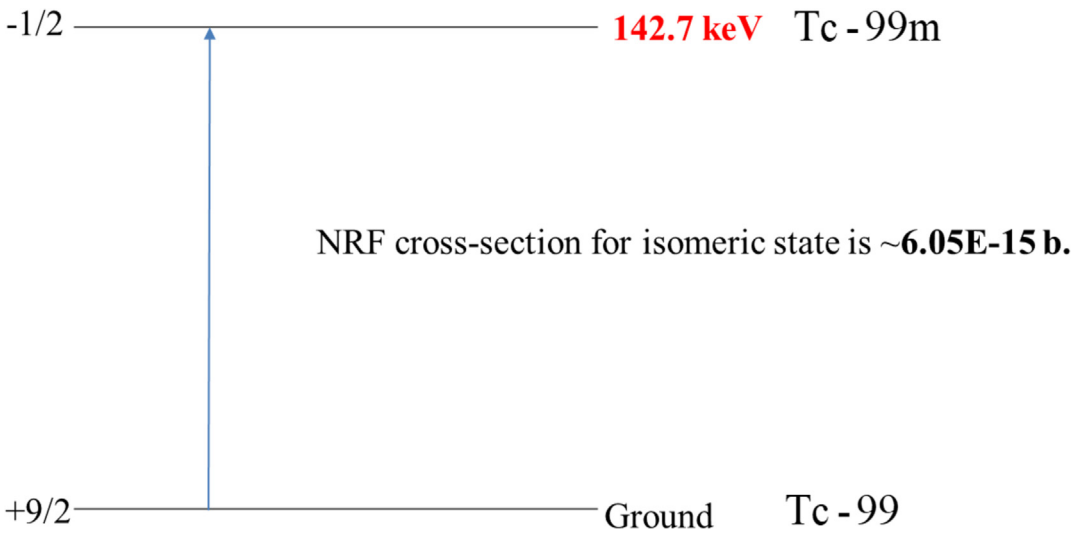

Fig. 2. Direct excitation from ground to Tc-99 m.

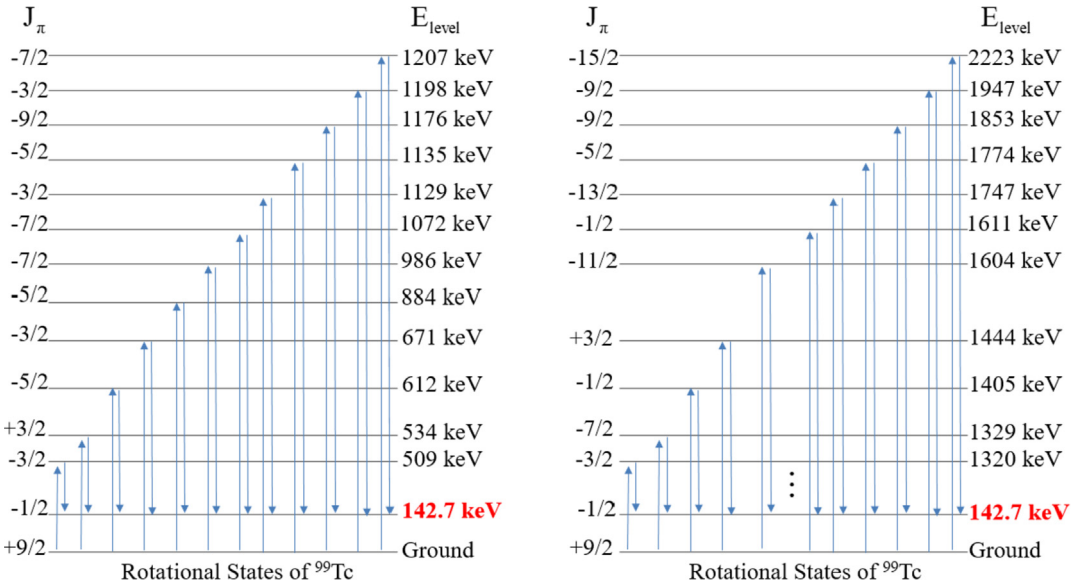

Fig. 3. Possible transition paths ways to produce ^{99m}Tc from the ground state of ^{99}Tc.

$$\frac{d\sigma}{sin\theta d\theta} = \pi r_0^2 \frac{\left(1-\beta^2\right)}{(1-\beta cos\theta)^2} R^2 \times \left(R + \frac{1}{R} - 1 + \cos^2\theta'\right) \tag{10}$$

where r_0 is the classical electron radius (2.818 fm) and θ' is the scattering angle in ER frame,

$$R = \frac{E_\gamma^{ER}}{E_L^{ER}} = \frac{1}{1 + \frac{E_L^{ER}}{mc^2}\left(1 + cos\theta'\right)} \tag{11}$$

$$E_L^{ER} = \frac{\sqrt{1-\beta^2}}{1-\beta} E_L \tag{12}$$

$$cos\theta' = \frac{cos\theta - \beta}{1 - \beta cos\theta} \tag{13}$$

The total photon scattering cross-section is obtained by integrating the differential Compton scattering cross-section for the cone angle θ_c and is given by Eq. (14):

$$\sigma(\theta_c) = \int_0^{\theta_c} \frac{d\sigma}{d\theta}\, d\theta \tag{14}$$

LCS gamma-rays can be used for photonuclear transmutation as they are energy-tunable, quasi-monochromatic, and beam-like. The intensity of the LCS gamma-rays should be strong for efficient and high nuclear conversion rate [14].

3.2. LCS facilities

Various LCS photon sources are being developed all over the world. Viable examples that are already in operation or under construction include the high intensity gamma-ray source (HIGS)

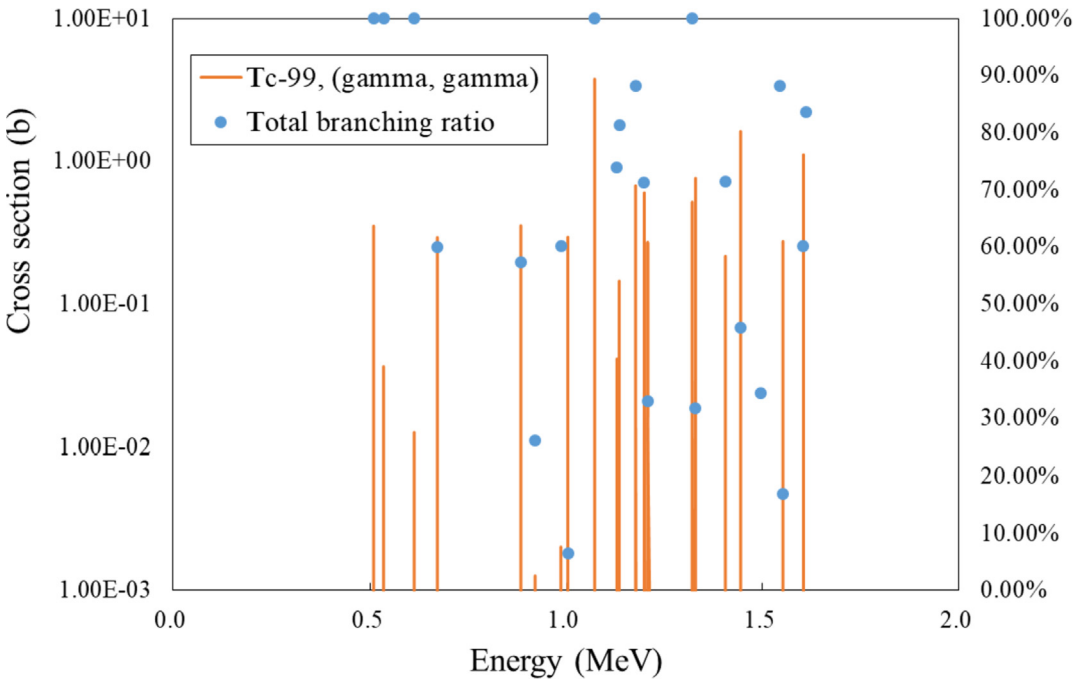

Fig. 4. NRF cross-sections at 300 K and BR_{total} for 21 excited states.

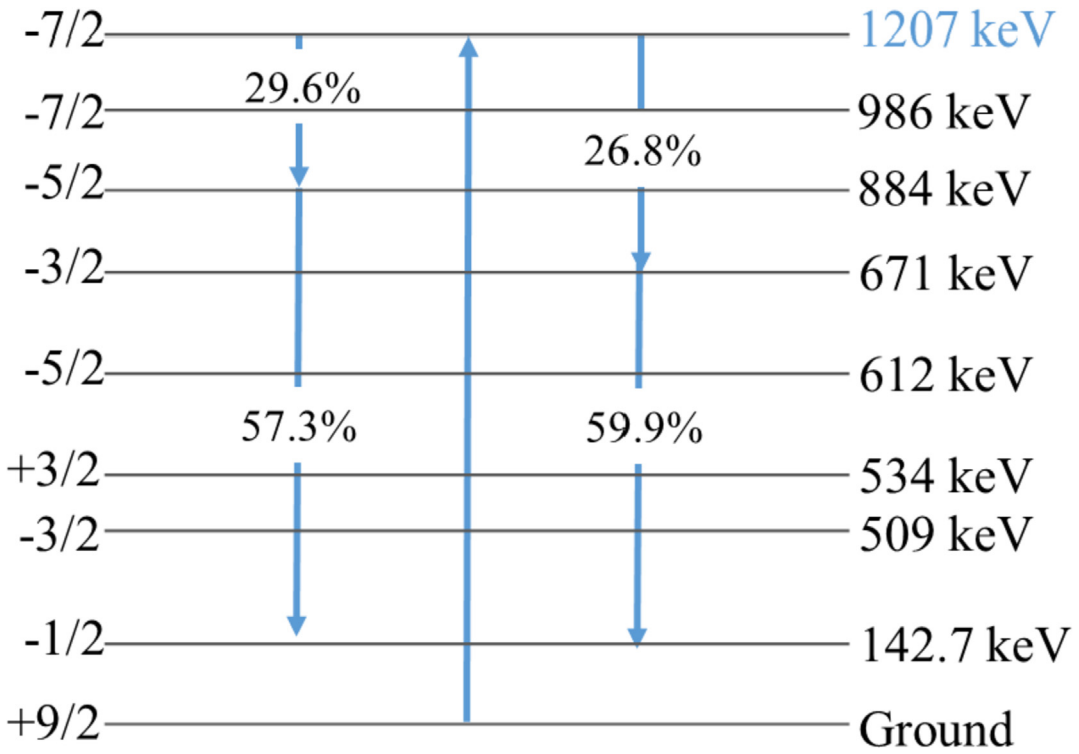

Fig. 5. Rotational energy states of ^{99}Tc nucleus.

facility at Duke University, the NewSUBARU in Japan, the mono-energetic gamma-ray (MEGA-ray) facility at the Lawrence Livermore national laboratory, the Shanghai laser electron gamma source (SLEGS) facility in China, and the extreme light infrastructure-nuclear physics (ELI-NP) facility of European collaboration. Table 3 presents the relevant features of these facilities. State-of-the-art facilities are able to produce the desired LCS gamma-rays with energies ranging from a few MeV to 100 MeV and intensities up to 10^{13} #/sec [15].

In this research, an LCS facility with an energy-recovery LINAC (ERL) system is considered as the gamma-ray source. T. Hayakawa et al. recently designed a high-flux LCS gamma-ray facility utilizing a 350 MeV ERL system [16]. The facility was reported to yield a gamma-ray intensity on the order of 10^{13} #/s. In the Hayakawa's

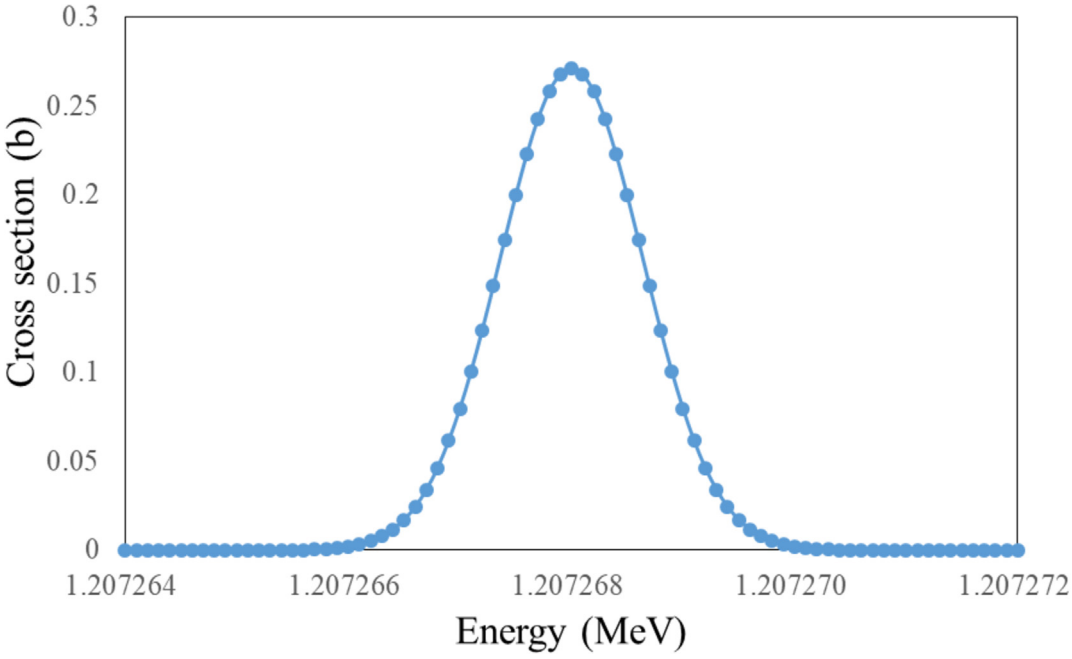

Fig. 6. The NRF cross-section for ^{99}Tc near 1207 keV.

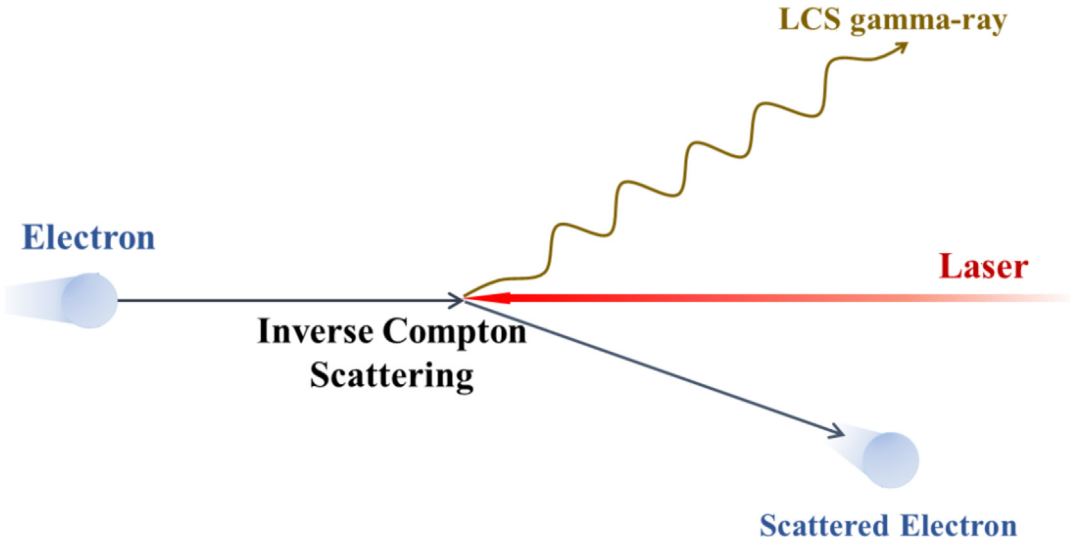

Fig. 7. Laser Compton scattering process.

ERL system, a 3-loop design is employed for cost reduction and compactness. An electron beam emitted from an injector is accelerated by a superconducting LINAC. After the three recirculation loops, the electron beam is re-injected into the LINAC with a deceleration phase, and the electron energy is fed back into the radio-frequency cavity of the superconducting LINAC. LCS gamma-rays are finally generated from the collisions of the electrons with the laser photons at the end of the loop.

4. Evaluation of photonuclear reaction of ^{99}Tc

The ^{99m}Tc production rate has been evaluated in two ways for efficient optimization of the initial LCS beam spectrum. First, the LCS spectrum is optimized without any self-shielding effects by photo-atomic interactions and NRF reaction in the ^{99}Tc target. Then, further optimizations are done by taking into account all self-shielding effects.

4.1. NRF reaction rate without any attenuation effects

Neglecting all photon attenuations including both the photo-atomic interactions and the NRF self-shielding effects, the NRF reaction rate can simply be estimated using Eq. (15):

$$N_{reac} = n_{\text{target}} \cdot d \cdot BR_{total} \int_{E}^{E_h} dE_\gamma \sigma_{NRF} \frac{dN_\gamma}{dE_\gamma} \tag{15}$$

where n_{target} is the number of atoms per cubic centimeter of the target material ^{99}Tc, d is the thickness of the target material, σ_{NRF} is

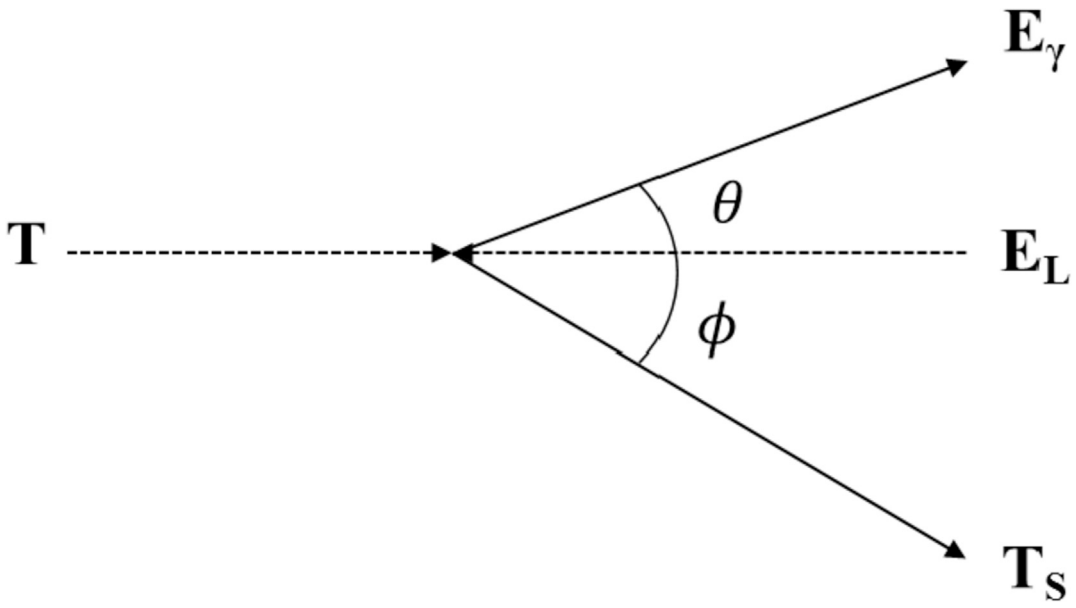

Fig. 8. Laser Compton scattering in laboratory frame.

Table 3
Existing LCS photon facilities.

Facility	Electron energy	Laser energy	LCS photon energy	Intensity (#/sec)
HIGS (In-service)	0.24–1.2 GeV	1.17–6.53 eV	1–100 MeV	10^7-2x10^{10}
NewSUBARU (In-service)	1.0 GeV	1.165 eV	≤17.6 MeV	10^7
MEGa-ray (Driving test)	250 MeV	2.33 eV	0.5–2.3 MeV	10^{12}
SLEGS (Under development)	3.5 GeV	0.117 eV	2–20 MeV	10^5–10^7
ELI-NP (Operation start in 2019)	600 MeV	2–5 eV	1–13 MeV	10^{13}

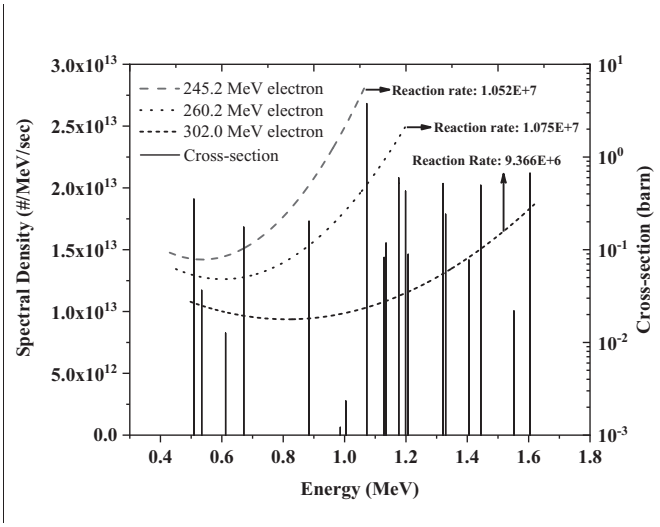

Fig. 9. ^{99}Tc NRF cross-sections and LCS spectrum-dependent total NRF reaction rate.

the NRF-based resonance cross-section, E_l and E_h is the lowest and highest energy of the LCS gamma-rays' photon spectrum, respectively, the dN_γ/dE_γ is the spectral density calculated using Eq. (16):

$$\frac{dN_\gamma}{dE_\gamma} = \frac{N_\gamma}{\sigma_t} \int_{E_0-\delta_E}^{E_0+\delta_E} \frac{d\sigma}{dE_\gamma} \frac{1}{\sqrt{2\pi}\delta_E} exp\left[-\frac{(E_e - E_0)^2}{2\delta_E^2}\right] dE_e \qquad (16)$$

where N_γ is the total gamma-ray intensity in the unit of #/sec, σ_t is the total Compton scattering cross-section in mb, $d\sigma/dE_\gamma$ is the differential Compton scattering cross-section with units of mb/MeV, E_0 is the central electron beam energy in MeV, and δ_E is the dispersion of the electron beam from its central energy value. In these calculations, δ_E is neglected and the difference is less than 10%. It is worthwhile to note that the spectral density is constant within the energy range of E_l and E_h as the energy range is less than 10 eV.

The designed electron energy is 350 MeV in the original ERL facility. However, the electron energy is decreased from 350 MeV to 302 MeV in this study because the required energy of LCS photon is reduced. The maximum energy of LCS photon is adjusted to 1.624 MeV because the NRF cross-section cannot be evaluated due to missing information above 1.624 MeV. Also the collimated angle is adjusted to 2.55 mrad, which is enough to cover all excited energy as well as preventing undesirable heating and other reactions. The target is assumed to be placed 50 cm from the LCS gamma-ray source. The target is considered to have cylindrical shape with 1 cm depth.

The LCS spectrum needs to be optimized in such a way to maximize total reaction rate in the 21 NRF resonances in Fig. 4. Three LCS spectra were considered in the optimization and Fig. 9 shows the results for 21 NRF cross-sections. The first intuition in maximizing the reaction rates is to cover all the 21 energy states with the LCS gamma ray spectrum. Therefore, the spectrum is obtained with an electron energy of 302 MeV and cone angle of 2.55 mrad as mentioned previously to obtain the reaction rates of ~9.37 × 10^6 (#/s). However, it can be seen from Fig. 9 that despite the fact all 21 energy states are covered by LCS spectrum, the spectral density is quite low for some of the energy states that can have significant impact (e.g., one appearing at 1.07 MeV) due to

their large integrated cross-sections (i.e., 5.37 eVb). To take into account this specific energy state, the electron energy was accordingly reduced. It has been shown in Fig. 9 that a lower electron energy of 260.2 MeV clearly provides a higher total reaction rate (~1.08×10^7 (#/s) than the original wider LCS spectrum. In Fig. 9, it is worthwhile to note that the total reaction rate is lower if the electron energy is lowered further, e.g., 245.2 MeV. Fig. 9 clearly demonstrates that the LCS beam spectrum should be appropriately narrow or wide to maximize the photo-production of ^{99m}Tc since a few or many NRF resonances can be involved in the NRF reaction.

Table 4 provides the NRF reaction rate at each resonance for the three LCS spectra considered in Fig. 9. It can be seen that individual NRF reaction rates are affected by different LCS spectrums. In addition, the energy state of 1.072 MeV is the biggest contributor in terms of the NRF reaction rate for all three LCS spectra due to its relatively large NRF cross-section.

4.2. NRF reaction rates with photo-atomic interaction

In this section, the impacts of photo-atomic reactions on the incident LCS gamma rays spectral density have been quantified using the MCNP6 code [17]. The photoelectric absorption and pair production contribute directly to the incident beam loss, while the Compton scattering process results in the energy change, leading to a softer and wider photon spectrum. The simulations have been performed considering the target geometry shown in Fig. 10. The ^{99}Tc target material is considered to be a cylinder of thickness 1 cm and the radius is assumed to be large enough so that all the gamma rays are absorbed within the target material.

The cylindrical target is further divided into ten equal-height sub-divisions for the analysis using MCNP6. The losses in LCS beam intensity and energy shifting in the spectral density due to the photo-atomic interactions, mainly the Compton scattering, are analyzed for the optimum LCS spectrum (E_e = 260.2 MeV) in Section 4.1 and is shown in Fig. 11.

In this analysis, it has been found that the initial source has undergone photoelectric absorption which is around 21% of the total photo-atomic interactions in the whole target, and the total beam intensity reduces noticeably. The pair production is negligibly small in the overall target region as the threshold energy is ~1.02 MeV. The reduction in the overall beam intensity due to pair production reaction is only about 0.007%. The Compton scattering does not reduce the beam intensity, however, it changes the photon energy depending on the scattering angle between the incident photon and orbital electron. It is observed that most of the Compton scattering interaction noticeably lower the energy of the incident photons. It is worthwhile to note that the Compton scattering results in an energy tail lower than the minimum energy bound of the initial source.

The change in the LCS gamma ray spectral density may lead to different NRF reaction rates and it is necessary to re-optimize the LCS spectrum. In this study, the re-optimization of LCS spectrum is performed by considering four different electron energies that 259.3 MeV, 263.2 MeV, 273.2 MeV, and 275.2 MeV, which are in the vicinity of the optimal energy in Section 4.1. Fig. 12 shows the region-wise spectral densities for the above-mentioned four different electron energies. One can note that the pair-production reaction results in a noticeable spike at ~0.511 MeV due to the positron-negatron annihilations.

Considering the impacts of photo-atomic reactions shown in Figs. 11 and 12, the NRF reaction rates can be re-calculated and the results are given in Table 5. It shows that the optimum electron energy is slightly higher (273.2 MeV) than that in Section 4.1 and the maximum total NRF reaction rate decreases by about 25% due to the LCS beam attenuation and spectrum softening resulting from the photo-atomic interactions.

4.3. NRF reaction rate with resonance self-shielding effect

For an accurate evaluation of a strong resonance reaction, it is necessary to consider a self-shielded energy spectrum. In this section, the NRF self-shielding effect is quantified using the resonance cross-section ($\sigma_{NRF)}$ given in Eq. (4). Taking into account the spectral density change due to the photo-atomic interactions (as shown in Figs. 11 and 12), the self-shielded spectral density dN_γ/dE_γ $_{(2)}$ is approximated in each resonance region by Eq. (17):

Table 4
Tc-99 m production rates for various NRF peaks at different electron energies.

Excited states (keV)	Reaction rate (#/sec)	Excited states (keV)	Reaction rate (#/sec)	Excited states (keV)	Reaction rate (#/sec)
E_e = 302 MeV		E_e = 260.2 MeV		E_e = 245.2 MeV	
509.1	1.63E+05	509.1	1.97E+05	509.1	2.17E+05
534.43	1.74E+04	534.43	2.12E+04	534.43	2.35E+04
612.37	6.53E+03	612.37	8.28E+03	612.37	9.51E+03
671.48	9.66E+04	671.48	1.28E+05	671.48	1.51E+05
884.259	1.44E+05	884.259	2.34E+05	884.259	3.08E+05
920.58	2.47E+02	920.58	4.17E+02	920.58	5.57E+02
986.17	9.98E+02	986.17	1.80E+03	986.17	2.47E+03
1004.07	1.97E+03	1004.07	3.63E+03	1004.07	5.00E+03
1072.23	3.55E+06	1072.23	6.97E+06	1072.23	9.80E+06
1129.105	8.55E+04	1129.105	1.76E+05	1129.105	0.00E+00
1135.04	1.24E+05	1135.04	2.56E+05	1135.04	0.00E+00
1176.48	6.70E+05	1176.48	1.43E+06	1176.48	0.00E+00
1198.89	5.03E+05	1198.89	1.09E+06	1198.89	0.00E+00
1207.26	1.06E+05	1207.26	2.32E+05	1207.26	0.00E+00
1320.732	7.59E+05	1320.732	0.00E+00	1320.732	0.00E+00
1329.404	3.60E+05	1329.404	0.00E+00	1329.404	0.00E+00
1405.454	1.33E+05	1405.454	0.00E+00	1405.454	0.00E+00
1444.134	9.18E+05	1444.134	0.00E+00	1444.134	0.00E+00
1552.12	4.97E+04	1552.12	0.00E+00	1552.12	0.00E+00
1604.287	1.67E+06	1604.287	0.00E+00	1604.287	0.00E+00
1611.376	7.91E-01	1611.376	0.00E+00	1611.376	0.00E+00

*G.S is an abbreviation of ground state.

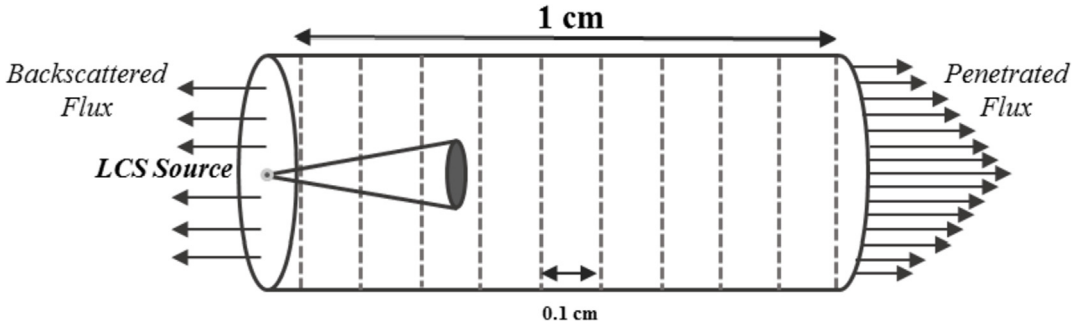

Fig. 10. ^{99}Tc cylindrical target geometry for the MCNP analysis.

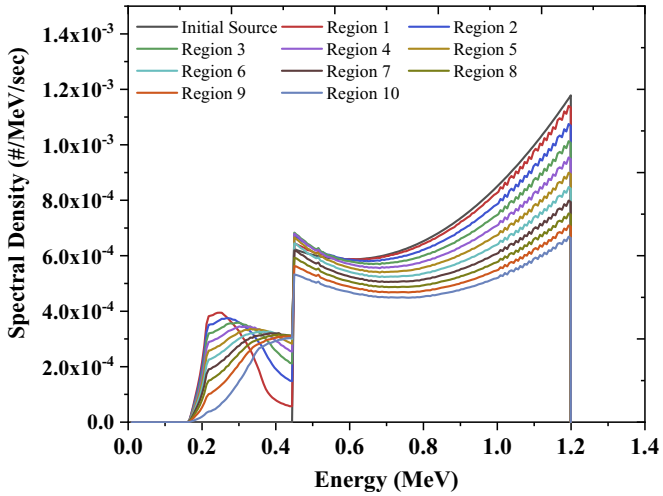

Fig. 11. Spectral density in each sub-region of the cylindrical target (E_e = 260.2 MeV).

$$\frac{dN_\gamma}{dE_{\gamma\,(2)}} = \frac{dN_\gamma}{dE_{\gamma\,(1)}}\, e^{-n_{\text{target}}\sigma_{\text{NRF}}(E)x_{\text{region}}} \tag{17}$$

where $dN_\gamma/dE_{\gamma\,(1)}$ is the spectral density accounting for the effect of photo-atomic interactions only and x_{region} is distance from the surface of the target.

To evaluate the NRF reaction rates in each 0.1 cm thick sub-region in Fig. 10, the spectral density $dN_\gamma/dE_{\gamma\,(1)}$ is multiplied by the self-shielding factor corresponding to x_{region} equal to the distance from the top of the target to midpoint of the sub-region. In each resonance region, the NRF reaction rate was calculated with Eq. (15) by dividing the small resonance width (40 eV) into 1000 equal intervals. Table 6 provides the final NRF reaction rates for several regions and important NRF peaks. The value in the parenthesis denotes the percentage decrease in NRF reaction rates as compared to the results with only photo-atomic attenuation. It is noted that the reaction rates are also affected by NRF self-shielding and its impact is enhanced when the cross-section of a resonance peak is relatively high, e.g., 1.072 MeV peak. The eventual reaction rates decreases by 28.5% as compared to reaction rates without any attenuations. The overall results are summarized in Table 7.

Table 8 provides the ^{99m}Tc activity with the currently used gamma-ray intensity of 10^{13} γ/s and an optimistic intensity of 10^{17} γ/s, which can be achievable in the future [18]. The reported results are calculated for the optimal LCS for E_e = 273.2 MeV in Table 7. The ^{99m}Tc activity given in Table 8 is produced for selected irradiation times with the knowledge that the time needed to achieve a secular equilibrium state is ~30 h. These intervals are selected to compare the production rate with irradiation time, which directly translates to operational cost in addition to time delay. Accounting for the fact that suggested activity of ^{99m}Tc for an average adult patient ranges from 0.1 to 30 mCi for various diagnostic indications, it is clear from Table 8 that LCS beam intensity should be much higher than the currently available one in terms of ^{99m}Tc activity. Table 8 provides that a high LCS beam intensity 10^{17} γ/s can result in a substantially high ^{99m}Tc activity depending on irradiation time. For example, activity for at least about 10 patients can be produced in an hour irradiation.

It is obvious that a high intensity Compton backscattering gamma sources is necessary for a high production rate of ^{99m}Tc. Various LCS facilities with a very high gamma flux are in design and construction phases and will be available in the near future, being an attractive option for the production of ^{99m}Tc. The attractiveness of these future facilities can be further enhanced by producing multiple LCS beams from a single electron beam using the multiple LCS beam extraction concept (MULEX) [19]. It should also be considered that a compact LCS facility can be located in big cities near hospitals, allowing for ^{99m}Tc to be produced on demand, thereby reducing its material losses due to proximity to the customers.

Based on the physics study and analysis, the photo-production of ^{99m}Tc using the NRF phenomenon seems to be a feasible option. However, despite all the benefits of the aforementioned process, the separation of produced ^{99m}Tc from the residual ^{99}Tc is a big technical challenge. In the conventional method, ^{99m}Tc is obtained from the ^{99m} Tc generators and relatively pure ^{99m}Tc is injected into the human body for medical diagnosis. This ^{99m}Tc decays into hazardous ground state ^{99}Tc. However, the activity due to ^{99}Tc in this case is known to be controlled at a very low level in the human body. In addition, most of the ^{99}Tc is removed from the body through feces. Meanwhile, it is unavoidable, in the proposed method, to inject a large amount of ^{99}Tc into human body with the current photo-production of ^{99m}Tc method since separation of ^{99}Tc from ^{99m}Tc is extremely difficult. This problem may be solved by increasing the production rate of ^{99m}Tc to an extent that the residual ^{99}Tc becomes insignificant, which requires an ultra-high intensity of the LCS beam and it is not considered to be a practical approach.

5. Conclusions

The proposed NRF-based photonuclear reaction is anticipated to innovate the production of the medical isotope ^{99m}Tc by recycling the long-living radioactive isotope ^{99}Tc from nuclear waste. It has been found that direct excitation of ground state ^{99}Tc to ^{99m}Tc is not effective due to a very small NRF cross-section. In case the ground state ^{99}Tc is excited to a higher energy level than that of the

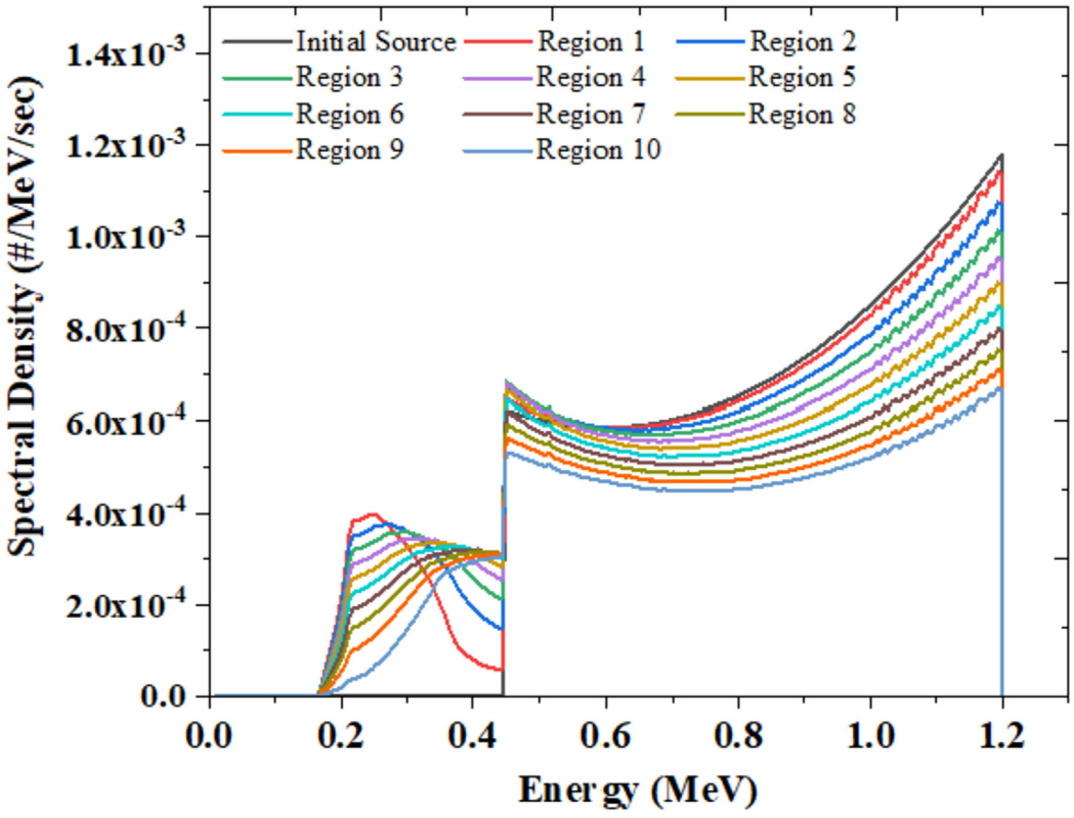

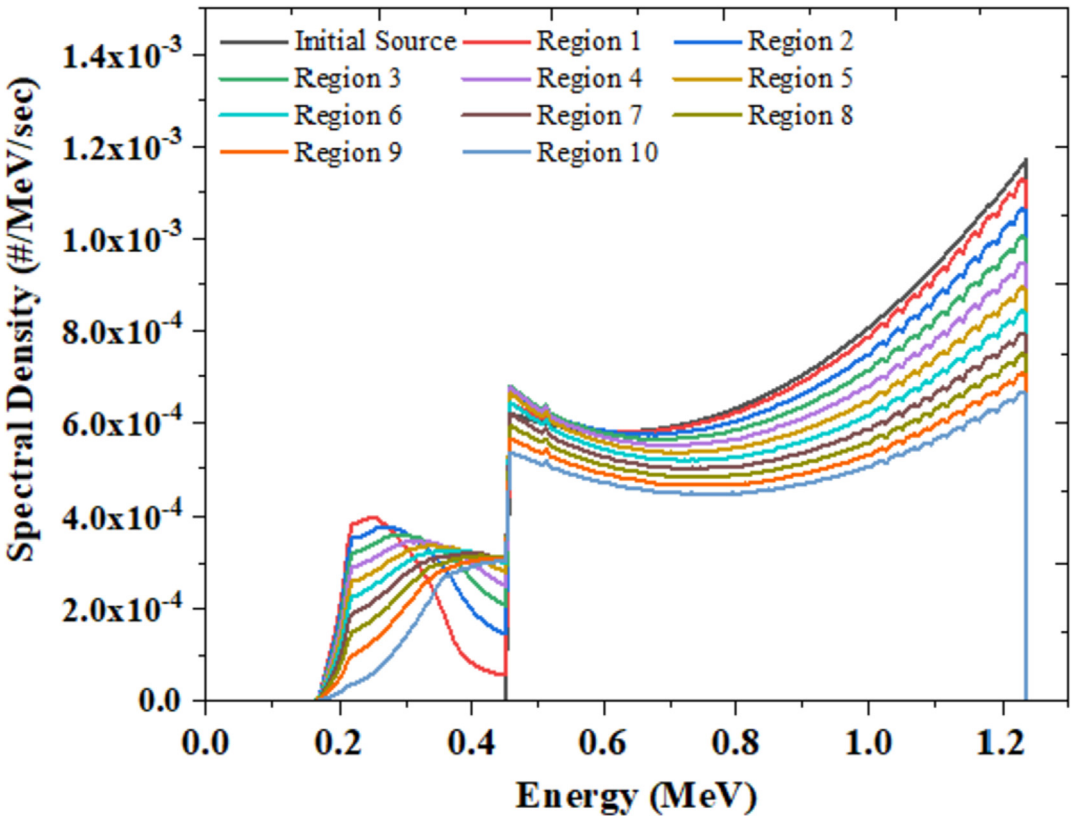

Fig. 12. a. Region-wise spectral density of the cylindrical target for $E_e = 259.3$ MeV.
b. Region-wise spectral density of the cylindrical target for $E_e = 263.2$ MeV.
c. Region-wise spectral density of the cylindrical target for $E_e = 273.2$ MeV.
d. Region-wise spectral density of the cylindrical target for $E_e = 275.2$ MeV.

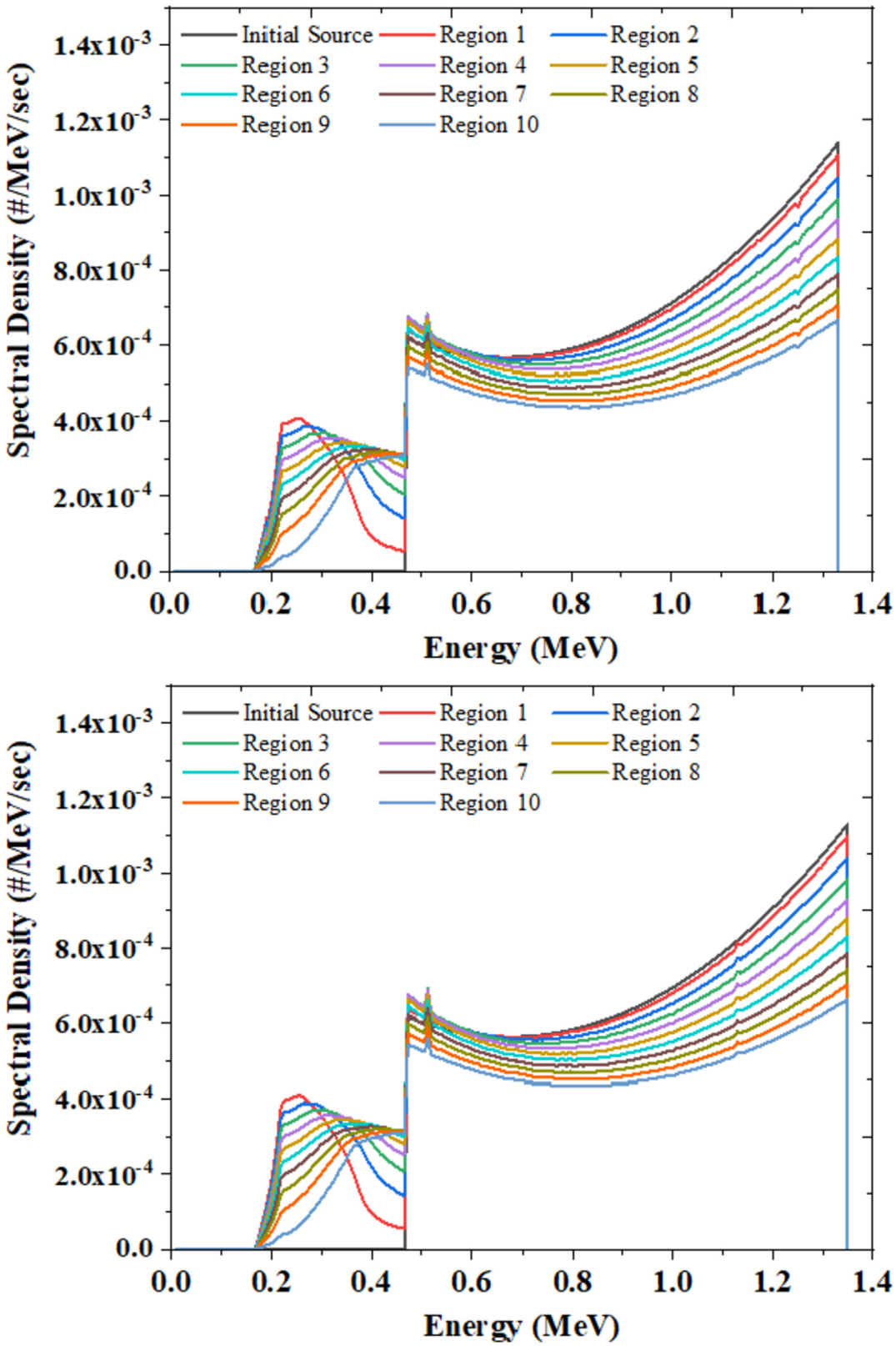

Fig. 12. (*continued*).

metastable technetium, ^{99m}Tc can be produced from subsequent decay of the excited nucleus. For an effective production of ^{99m}Tc, the LCS beam intensity should be as high as 10^{17} γ/s due to small NRF cross-sections of ^{99}Tc. Even with an optimistic LCS beam strength, it has been found that a very small fraction of target ^{99}Tc is transmuted to ^{99m}Tc. Both the photo-atomic interactions of the LCS photons and NRF self-shielding itself should be accounted for accurate evaluation of the NRF reaction rate. The results in this work

Table 5
Impacts of the photo-atomic reactions on NRF reaction rates.

Region No.	Reaction Rates (#/s)				
	$E_e = 259.3$ MeV	$E_e = 260.2$ MeV	$E_e = 263.2$ MeV	$E_e = 273.2$ MeV	$E_e = 275.2$ MeV
1	9.866×10^5	9.828×10^5	9.379×10^5	9.750×10^5	9.410×10^5
2	9.392×10^5	9.357×10^5	8.935×10^5	9.348×10^5	8.973×10^5
3	8.937×10^5	8.943×10^5	8.547×10^5	8.929×10^5	8.646×10^5
4	8.506×10^5	8.499×10^5	8.111×10^5	8.537×10^5	8.251×10^5
5	8.076×10^5	8.087×10^5	7.720×10^5	8.162×10^5	7.870×10^5
6	7.647×10^5	7.684×10^5	7.374×10^5	7.784×10^5	7.548×10^5
7	7.292×10^5	7.323×10^5	7.004×10^5	7.445×10^5	7.189×10^5
8	6.886×10^5	6.937×10^5	6.673×10^5	7.138×10^5	6.884×10^5
9	6.573×10^5	6.601×10^5	6.333×10^5	6.774×10^5	6.563×10^5
10	6.224×10^5	6.273×10^5	6.025×10^5	6.443×10^5	6.253×10^5
Total	$\mathbf{7.940 \times 10^6}$	$\mathbf{7.953 \times 10^6}$	$\mathbf{7.610 \times 10^6}$	$\mathbf{8.031 \times 10^6}$	$\mathbf{7.759 \times 10^6}$

Table 6
Resonance-wise NRF reaction rates considering all shielding effects.

Excited states (keV)	Reaction Rates (#/s) with 273.2 MeV electron					
	Region 1		Region 5		Region 10	
509.1	1.893×10^4	(0.080%)[a]	1.964×10^4	(0.714%)	1.650×10^4	(1.500%)
534.43	1.939×10^3	(0.008%)	1.973×10^3	(0.074%)	1.705×10^3	(0.157%)
612.37	7.358×10^2	(0.003%)	7.225×10^2	(0.026%)	6.282×10^2	(0.054%)
671.48	1.107×10^4	(0.040%)	1.056×10^4	(0.357%)	9.132×10^3	(0.751%)
884.259	1.844×10^4	(0.046%)	1.625×10^4	(0.412%)	1.348×10^4	(0.868%)
920.58	3.236×10^1	(0.000%)	2.827×10^1	(0.001%)	2.336×10^1	(0.001%)
986.17	1.366×10^2	(0.000%)	1.173×10^2	(0.002%)	9.524×10^1	(0.005%)
1004.07	2.729×10^2	(0.001%)	2.330×10^2	(0.005%)	1.885×10^2	(0.010%)
1072.23	$\mathbf{5.083 \times 10^5}$	**(0.850%)**	$\mathbf{3.992 \times 10^5}$	**(7.358%)**	$\mathbf{2.923 \times 10^5}$	**(14.81%)**
1129.105	1.274×10^4	(0.019%)	1.058×10^4	(0.168%)	8.299×10^3	(0.354%)
1135.04	1.849×10^4	(0.027%)	1.531×10^4	(0.240%)	1.200×10^4	(0.506%)
1176.48	1.024×10^5	(0.135%)	8.340×10^4	(1.205%)	6.418×10^4	(2.524%)
1198.89	7.772×10^4	(0.097%)	6.333×10^4	(0.871%)	4.871×10^4	(1.828%)
1207.26	1.650×10^4	(0.020%)	1.351×10^4	(0.182%)	1.045×10^4	(0.384%)
1320.732	1.236×10^5	(0.117%)	9.914×10^4	(1.049%)	7.467×10^4	(2.200%)
1329.404	5.889×10^4	(0.055%)	4.743×10^4	(0.492%)	3.592×10^4	(1.034%)
Total	$\mathbf{9.702 \times 10^5}$	**(0.491%)**	$\mathbf{7.814 \times 10^5}$	**(4.274%)**	$\mathbf{5.883 \times 10^5}$	**(8.692%)**

[a] Percentage decrease due to the NRF self-shielding effect.

Table 7
NRF reaction rates with different evaluation schemes.

Schemes	Reaction Rates (#/s)				
	$E_e = 259.3$ MeV	$E_e = 260.2$ MeV	$E_e = 263.2$ MeV	$E_e = 273.2$ MeV	$E_e = 275.2$ MeV
Without attenuations	1.072×10^7	1.075×10^7	1.011×10^7	1.030×10^7	9.929×10^6
Photo-atomic attenuation only	7.940×10^6	7.953×10^6	7.610×10^6	8.031×10^6	7.759×10^6
With all shielding effects	7.531×10^6	7.551×10^6	7.225×10^6	7.683×10^6	7.422×10^6

Table 8
Activity in the unit of mCi[a] as a function of irradiation time.

Irradiation time (hr)		1	6	12	24	30	48
10^{13} γ/s	Tc-99 m	0.023	0.104	0.155	0.195	0.201	0.207
	Tc-99	9.61	9.61	9.61	9.61	9.61	9.61
10^{17} γ/s	Tc-99 m	225.8	1036	1555	1946	2011	2068
	Tc-99	9.61	9.61	9.61	9.61	9.61	9.61

[a] 1 Ci = 3.7×10^{10}Bq.

demonstrate the potential possibility of ^{99}Tc recycling, thus relieving the woes of nuclear waste management. Nevertheless, taking into account difficulty in separation of ^{99m}Tc from the residual ^{99}Tc, we conclude that the proposed photo-production of ^{99m}Tc may not be suitable for actual clinical application in the near future.

Acknowledgements

We would like to acknowledge with gratitude the technical help of Dr. Tatsuhiko Ogawa of Japan Atomic Energy Agency (JAEA). This research was partially supported by Korea Hydro and Nuclear Power Co., Ltd.

References

[1] A. Fong, T. Meyer, K. Zala, Making Medical Isotopes: Report of the Task Force on Alternatives for Medical-isotope Production. TRIUMF, Vancouver, 2008.
[2] Diamond, W., NIM A, 1999(432).
[3] NEA/OECD, The Supply of Medical Radioisotopes: Review of Potential Molybdenum-99/technetium-99m Production Technologies, 2010.
[4] X. Hou, et al., Theoretical dosimetry estimations for radioisotopes produced by proton-induced reactions on natural and enriched molybdenum targets, Phys. Med. Biol. 57 (6) (2012) 1499.
[5] O. Lebeda, et al., Assessment of radionuclidic impurities in cyclotron produced 99m Tc, Nucl. Med. Biol. 39 (8) (2012) 1286–1291.
[6] J. Lee, Photoproduction of ^{99}mTc with Laser-Compton Scattering Gamma-ray, Master Thesis, Korea Adv. Inst. Science, Techn., Daejeon, Republic of Korea, 2016.
[7] A. Sandorfi, et al., The fabrication of a Very High Energy Polarized Gamma Ray Beam Facility and a Program of Medium Energy Physics Research at the National Synchrotron Light Source, 1982. Brookhaven National Laboratory Report BNL-32717, BNL Physics Department, Proposal to the Department of Energy.
[8] J. Stepanek, Parametric study of laser Compton-backscattering from free relativistic electrons, Nucl. Instrum. Methods Phys. Res. Sect. A Accel. Spectrom. Detect. Assoc. Equip. 412 (1) (1998) 174–182.
[9] T. Ogawa, S. Hashimoto, T. Sato, Development of general nuclear resonance fluorescence model, J. Nucl. Sci. Technol. 53 (11) (2016) 1766–1773.
[10] T. Sato, et al., Particle and heavy ion transport code system, PHITS, version 2.52, J. Nucl. Sci. Technol. 50 (9) (2013) 913–923.
[11] Data extracted using the NNDC On-Line Data Service from the ENSDF database, file revised as of (2017) M.R. Bhat, Evaluated Nuclear Structure Data File (ENSDF), in: S.M. Qaim (Ed.), Nuclear Data for Science and Technology, SpringerVerlag, Berlin, Germany, 1992, p. 817.
[12] J.lvi Blatt, V.F. Weisskopf, Theoretical Nuclear Physics, John Wiley and Sons, lnc., New York, 1952.
[13] R.B. Firestone, V.S. Shirley, C.M. Baglin, Table of isotopes CD-ROM, 1996, p. 1. Eight Edition Version.
[14] ur Rehman, H.,J. Lee, Y. Kim, Optimization of the laser-Compton scattering spectrum for the transmutation of high-toxicity and long-living nuclear waste, Ann. Nucl. Energy 105 (2017) 150–160.
[15] http://accelconf.web.cern.ch/accelconf/ipac2012/talks/tuxb03_talk.pdf.
[16] T. Hayakawa, et al., Nondestructive assay of plutonium and minor actinide in spent fuel using nuclear resonance fluorescence with laser Compton scattering γ-rays, Nucl. Instrum. Methods Phys. Res. Sect. A Accel. Spectrom. Detect. Assoc. Equip. 621 (1) (2010) 695–700.
[17] J.T. Goorley, M. James, T. Booth, MCNP6 User's Manual, Version 1.0. LA-CP-13–00634, Los Alamos National Laboratory, 2013.
[18] M. Shimada, R. Hajima, Inverse Compton scattering of coherent synchrotron radiation in an energy recovery linac, Phys. Rev. Spec. Top. Accel. Beams 13 (10) (2010) 100701d.
[19] H.U. Rehman, J. Lee, Y. Kim, Comparison of the laser-Compton scattering and the conventional Bremsstrahlung X-rays for photonuclear transmutation, Int. J. Energy Res. 42 (no. 1) (2018) 236–244.